Check for updates

Original Research

Advances in Structural Engineering

Advances in Structural Engineering
1–14
© The Author(s) 2018
Article reuse guidelines:
sagepub.com/journals-permissions
DOI: 10.1177/1369433218796407
journals.sagepub.com/home/ase
SAGE

Effect of axial compression ratio on concrete-filled steel tube composite shear wall

Hetao Hou[1,2], Weiqi Fu[1], Canxing Qiu[1], Jirun Cheng[1], Zhe Qu[2], Wencan Zhu[1] and Tianxiang Ma[1]

Abstract

This study proposes a new type of shear wall, namely, the concrete-filled steel tube composite shear wall, for high performance seismic force resisting structures. In order to study the seismic behavior of concrete-filled steel tube composite shear wall, cyclic loading tests were conducted on three full-scale specimens. One conventional reinforced concrete shear wall was included in the testing program for comparison purpose. Regarding the seismic performance of the shear walls, the failure mode, deformation capacity, bearing capacity, ductility, hysteretic characteristics, and energy dissipation are key parameters in the analysis procedure. The testing results indicated that the bearing capacity, the ductility, and the energy dissipation of the concrete-filled steel tube composite shear walls are greater than that of conventional reinforced concrete shear walls. In addition, the influence of axial compression ratio on the seismic behavior of concrete-filled steel tube composite shear wall is also investigated. It was found that higher axial compression ratio leads to an increase in the bearing capacity of concrete-filled steel tube composite shear walls while a reduction in the ductility capacity.

Keywords

axial compression ratio, composite shear wall, concrete-filled steel tube, quasi-static test, seismic behavior

Introduction

Reinforced concrete shear walls (RCSWs) are the core component in resisting the seismic force in high-rise buildings (Cao et al., 2003; Zhang et al., 2014). At present, the most popular shear walls (SWs) are usually casted in place during the construction. With the development of construction industrialization, precast concrete systems are gaining increasingly more applications. The use of precast concrete systems offers several advantages such as speedy erection, higher quality, lower project cost, better sustainability, and enhanced occupational health and safety (Polat, 2008). The earliest precast RCSWs are large panel precast concrete walls (Clough et al., 1989), and then they were developed to the unbounded post-tensioned precast SWs and precast composite SWs (Wang and Lv, 2010).

Regarding the precast composite SW, it consists of two precast concrete slabs and boundary restraints. The two precast concrete slabs are connected by the rebar truss, and they can be used as the forms with the precast boundary restraints to enclose a cavity in the middle of the wall plate. When the precast components are fixed at the construction site, the concrete can be poured into the cavity and the vertical rebars can be connected directly to the adjacent members. Such a construction procedure significantly reduces the in-situ work. Precast composite SWs combine the advantages of excellent overall performance of cast-in-place RCSWs and the high industrialization of precast RCSWs and have become the research focus of precast RCSWs in China (Wang and Lv, 2010). In fact, the past years witnessed a large amount of research and development of such kind of precast RCSWs. In particular, the seismic behavior of this structural system is the key factor that influences its application and extension (Priestley and Tao, 1993). The relevant studies show that the precast composite SWs have the comparable seismic behavior with the cast-in-place RCSWs. Xiao and Guo (2014) proved that the displacement ductility, stiffness degradation and energy dissipation

[1]School of Civil Engineering, Shandong University, Jinan, China
[2]Institute of Engineering Mechanics, China Earthquake Administration, Sanhe, China

Corresponding author:
Canxing Qiu, School of Civil Engineering, Shandong University, No. 17923, Jingshi Road, Jinan 250100, Shandong, China.
Email: qiucanxing@sdu.edu.cn

capacity of precast superimposed slab walls were close to those of cast-in-place SWs.

With the aim to improve the seismic behavior of precast composite SWs and to further improve the construction efficiency, this study introduces concrete-filled steel tubes (CFSTs) as the boundary restraints for CSWs to form a new type of CSW, namely, CSFT-CSW. The combination of concrete and steel in the SWs can give full play to the advantages of two materials. In fact, a few researchers have proposed similar ideas in recent years, and they can be divided into several categories. The first one is steel-reinforced concrete (SRC) SWs which add shaped steel or steel tubes in the boundary of SWs (Hu et al., 2016; Liao et al., 2012); the second one is to include single or double steel plates in the SWs (Eom et al., 2009; Hossain and Wright, 2004; Luo et al., 2015); the third one comprises steel frame boundary and infilled RC walls (Liao et al., 2009); and others such as bundled lipped channel-concrete (BLC-C) composite walls (Chen et al., 2016) and SWs with concealed bracing (Cao et al., 2003, 2006) were also discussed. Extensive studies have shown that the bearing capacity, energy dissipation capacity, and ductility of those steel–concrete composite SWs are better than those of cast-in-place RCSWs. The use of steel can increase the out-of-plane stiffness and improve the performance of compression zone in the plane. Besides, using steel to replace longitudinal reinforcement can not only improve the mechanical properties of the wall limb but also simplify the construction procedures, so it is promising to use it in practical applications.

At present, relevant studies on those steel–concrete composite SWs mainly focus on the cast-in-place RCSWs and seldom use it in precast composite SWs. To this end, this study carried out a series of cyclic loading tests to study the seismic performance of CSFT-CSWs which combined the steel–concrete composite SWs with precast composite SWs and tried to provide some inspirations for engineering application.

According to ACI 318-14 (2014), axial compression ratio is an important controlling factor in the seismic design of SW. Many studies have been carried out to investigate the effect of parameter variation of axial compression ratio on the behavior of RCSWs and indicated that axial compression ratio has an important effect on the failure mode, stiffness, and ductility of the walls (Looi et al., 2017; Zhang and Wang, 2000). Therefore, this study selects the axial compression ratio as the primary parameter.

Experimental program

Specimens

A total of four full-scale specimens were fabricated and tested in this experimental study. The SWs were labeled SW-1 through SW-4, in which SW-1 was a typical cast-in-place RCSW, whereas SW-2–SW-4 were CFST-CSWs. Figure 1 illustrates the schematic view of CFST-CSWs. The specimens are 3.0-m tall, 1.2-m wide, and 0.2-m thick. The cross-section of boundary columns is 200 mm × 200 mm. The shear-to-span ratio equals to 2.38. The dimensions and details of the

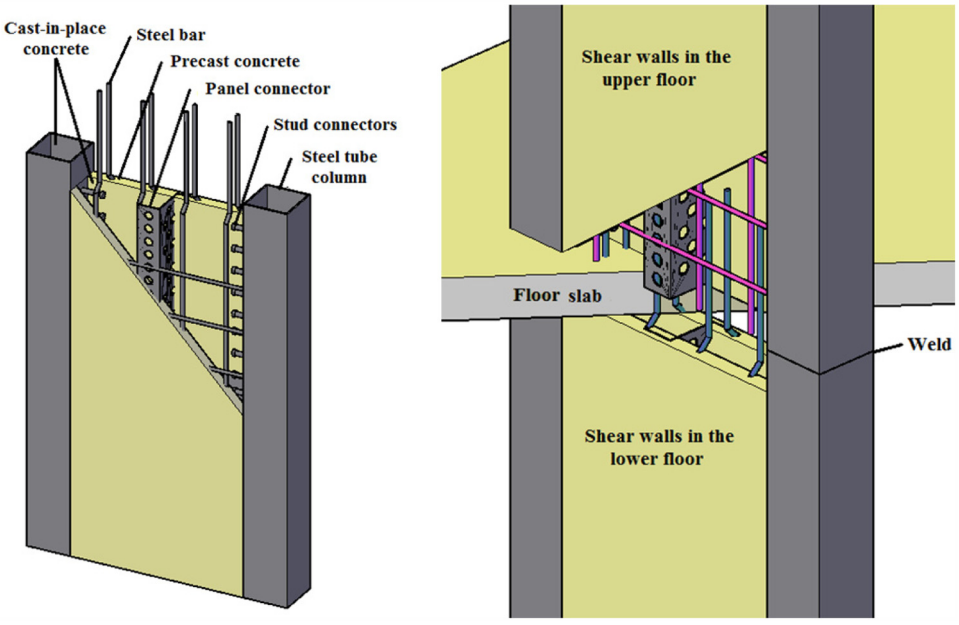

Figure 1. Schematic view of CFST-CSWs.

testing specimens are shown in Figure 2. For the boundary columns of specimen SW-1, the reinforcement ratio and stirrup ratio are 2.01% and 0.91%, respectively. Regarding with specimens SW-2–SW-4, the steel ratio, defined as the ratio of sectional area of steel tube to that of boundary column, is 8.80%. The core plate between the boundary components has a vertical reinforcement ratio of 0.57% and a horizontal reinforcement ratio of 0.41%. A reinforced concrete (RC) foundation beam with a cross-section of 600 by 1000 mm and an RC top beam with a cross-section of 200 by 800 mm were cast together with the wall. The horizontal reinforcements in the wall were welded to the steel tubes.

Material properties

The material properties of concrete and steel were tested before the formal testing of SW specimens. The concrete used in the specimens has strength grade C30, which has a nomimal cubic compressive strength f_{cu} = 30 MPa. The actual cubic compressive strength

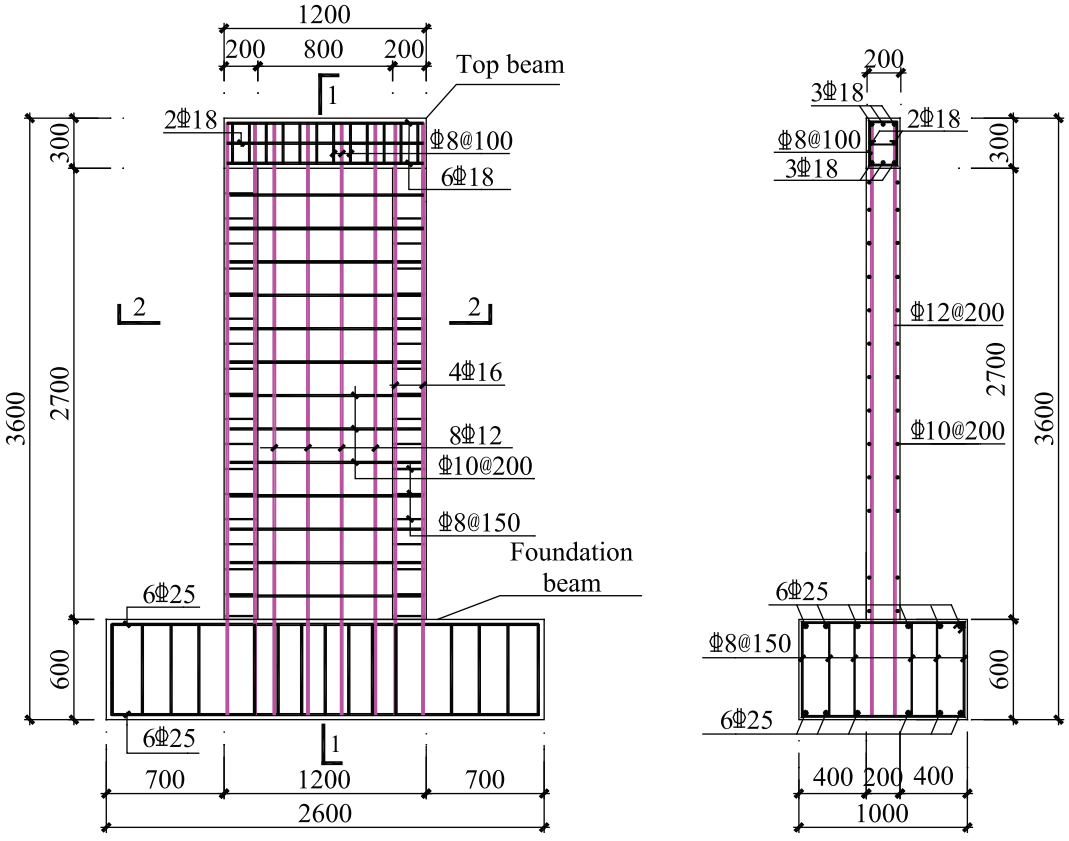

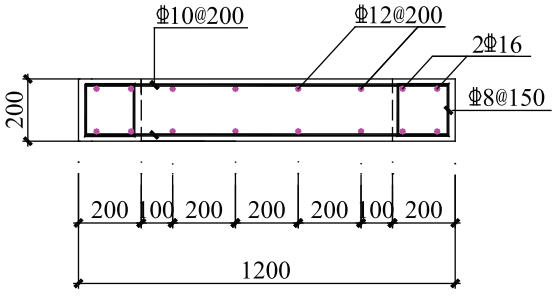

(a)

Figure 2. (continued)

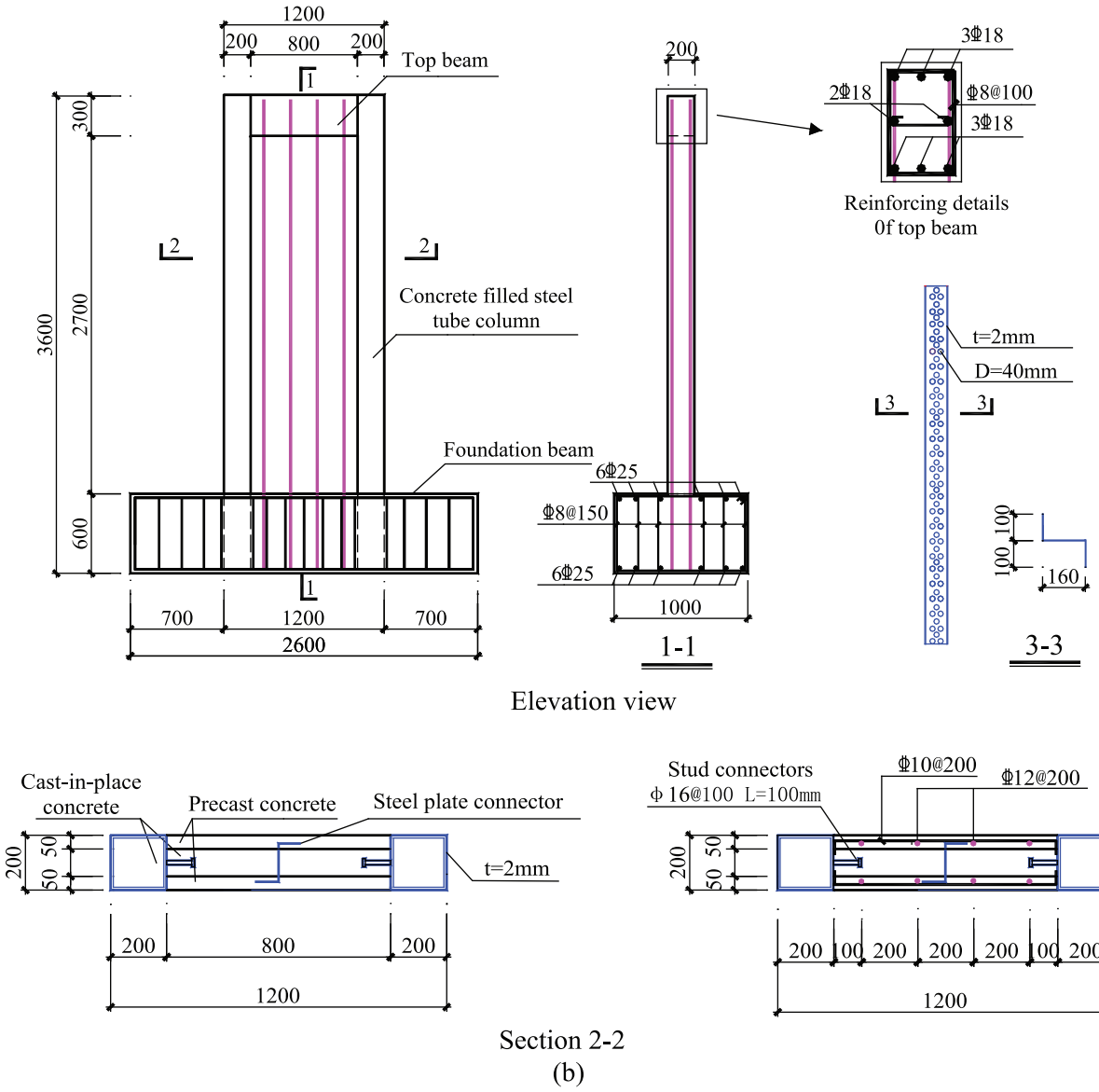

Figure 2. Dimensions and reinforcement distributions of specimens (unit: mm): (a) SW-1 and (b) SW-2/3/4.

Table 1. Dimension and properties of steel.

Strength grade	Diameter (thickness; mm)	Yield strength $f_{yt,}$ (MPa)	Ultimate strength $f_{ut,}$ (MPa)	Young's modulus $E_{s,}$ (10^5 MPa)
HRB400	D8	481.02	615.85	2.01
HRB400	D10	469.50	621.00	1.95
HRB400	D12	465.54	580.33	1.98
HRB400	D 16	563.33	643.33	2.00
Q235B	4.5	306.87	432.89	2.05

of precast concrete and cast-in-place concrete are 47.6 and 32.75 MPa, respectively. The rebars are deformed steel bars with a strength grade of HRB400 (nominal yield strength f_y = 400 MPa). The embedded structural steel has a strength grade of Q235 (f_y = 235 MPa). Table 1 summarizes the measured tensile yield strength $f_{y,t}$ and ultimate strength f_{ut} for the steel rebars and structural steel.

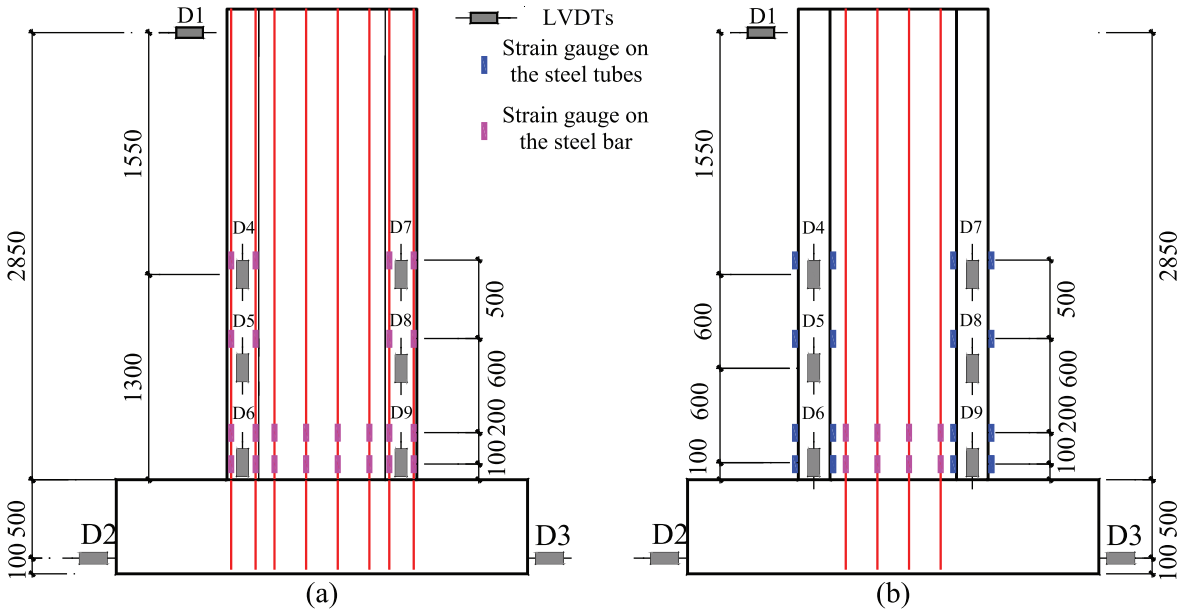

Figure 3. Layout of LVDTs and strain gauges (dimension unit: mm): (a) SW-1 and (b) SW-2/3/4.

Instrumentation

Instrumentation on the specimens was developed to record resistance, displacements, and strains of the specimens. Load cells were adopted to measure the vertical and lateral loads applied to the specimen. Figure 3 shows the locations of displacement transducers and strain gauges attached to the specimens. Nine linear variable differential transformers (LVDTs), which are designated as D1 through D9 in Figure 3, were used to measure the deformations of each specimen. Specifically, D1 measured the top displacement; D2 and D3 monitored slip of the footing relative to the strong floor (if any); D4 to D9 recorded the deformation between the boundary restraints and wall panels. Strain gauges were mounted on the embedded structural steel and vertical rebars, as shown in Figure 3.

Test setup and loading protocol

Figure 4 shows the test setup used in this investigation. Each specimen was fixed to the strong floor through high-strength bolts penetrating the footing. Two actuators exert the vertical and lateral loads, respectively, to the specimen through the top beam. To achieve a relatively uniform force distribution along the top beam, a rigid steel beam was placed between the top beam and vertical actuator. Out-of-plane restraints were provided at the top of each specimen. The vertical load was exerted to the specimen prior to application of the lateral load, and it was maintained to be constant during each test. Note that the connection between the vertical actuator and the beam of the reaction frame allows small rotations of the vertical actuator and thus enables the vertical load applied to each specimen to remain constant during the test.

The loading history is shown in Figure 5. The lateral loading was displacement controlled all the time. There are seven grade displacement levels which are determined by GB50011-2010 (2010) and Japan Building Standards Law (2002). The increasing peak displacements of each loading cycle correspond to the critical drift angles of conventional RC structures associated with the following key performance targets: namely a preloading drift (at the drift angle of 1/2000); the elastic story drift limit of RCSW structure (at the drift angle of 1/1000); the elastic story drift limit of RC frame structure (at the drift angle of 1/550); the story drift limit of the second anti-seismic level (at the drift angle of 1/200); the plastic story drift limit of RCSW structure (at the drift angle of 1/120); the plastic story drift limit of RC frame structure (at the drift angle of 1/50); and an arbitrarily selected drift limit of 1/30. Each loading level consisted of one cycle except that the loading levels with the peak drifts of 1/1000 and 1/120 consisted of two cycles. The push and pull forces from the horizontal actuator were assumed to be positive and negative, respectively. The test was terminated when degradation of the specimen lateral strength at the peak deformation of a certain cycle exceeds 15%.

The axial compression ratio, n, which represents the ratio of the design value of the axial load to the product of the compressive strength and sectional area, is a key design parameter in the test, and it is defined as below

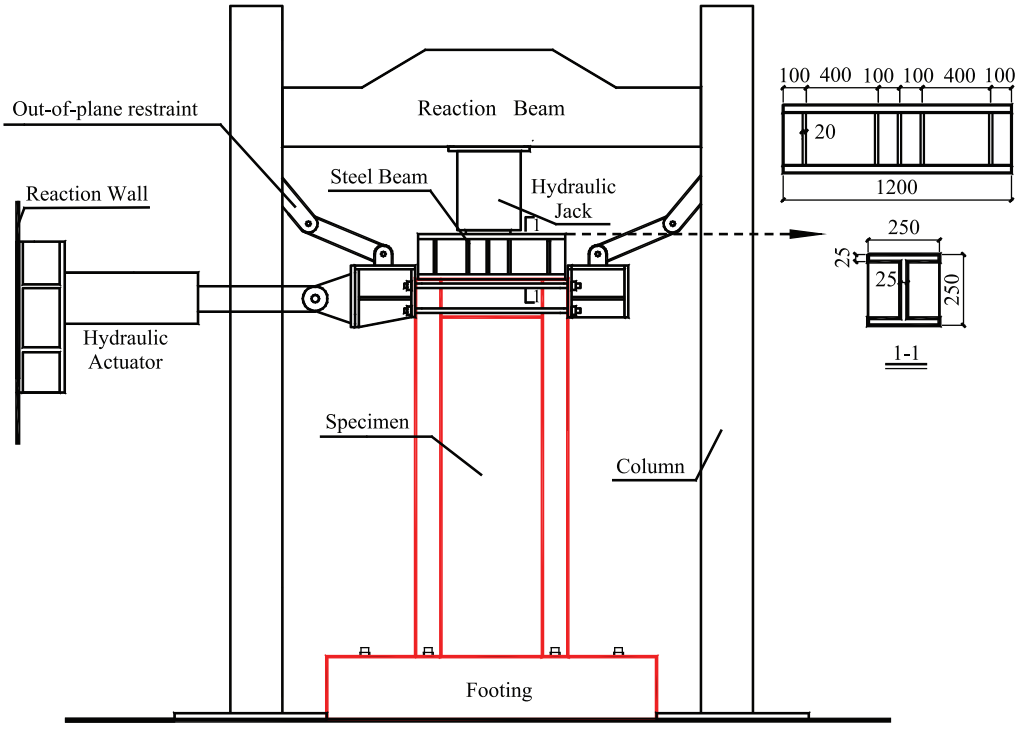

Figure 4. Test setup (unit: mm).

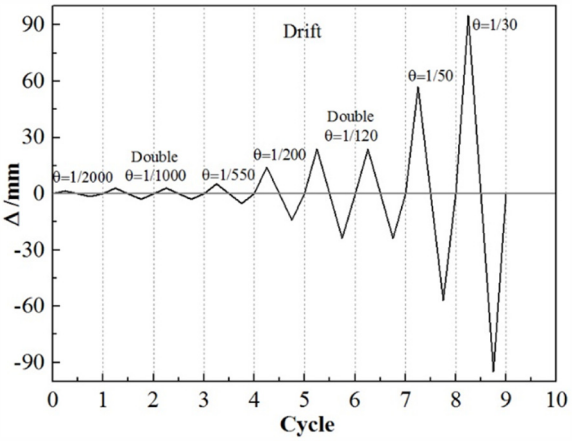

Figure 5. Loading history.

$$n = \frac{\alpha N}{A_c f_c + A_{cc} f_{cc} + A_a f_a} \quad (1)$$

where N is the applied vertical load on the wall; f_c and f_{cc} are the compressive strength of the cast-in-place and precast concrete; A_c and A_{cc} are the cross-sectional area of the cast-in-place and precast concrete. f_a and A_a are the yield strength and cross-sectional area of the steel tubes. The axial compression ratio of all specimens are listed in Table 2. To calculate the experiment axial compression ratio, α is 1.0, and the strength of concrete and steel is the measured value. It is seen that the axial compression ratio of CFSW-CSW is smaller than that of conventional SW when they are subjected to identical vertical load, due to the contribution of steel tubes, which implies the steel tubes improve the vertical loading capacity for the SW. To calculate the axial compression ratio in the design procedure, according to the method given by the Chinese seismic design code GB 50011-2010, α is 1.2, which represents the ratio of the design value of the axial load to the actual value in this test, and the strength of concrete and steel is the design value. Thus, the design value of axial compression ratio is also calculated, as listed in Table 2. It is seen that the maximum axial compression ratio is 0.61, which is larger than that required by GB 50011-2010. So the

Table 2. Axial compression ratio of specimens.

Specimen no.	The experiment axial compression ratio	The design axial compression ratio	Axial compression force (kN)
SW-1	0.15	0.36	1031
SW-2	0	0	0
SW-3	0.15	0.33	1363
SW-4	0.28	0.61	2536

SW: shear wall.

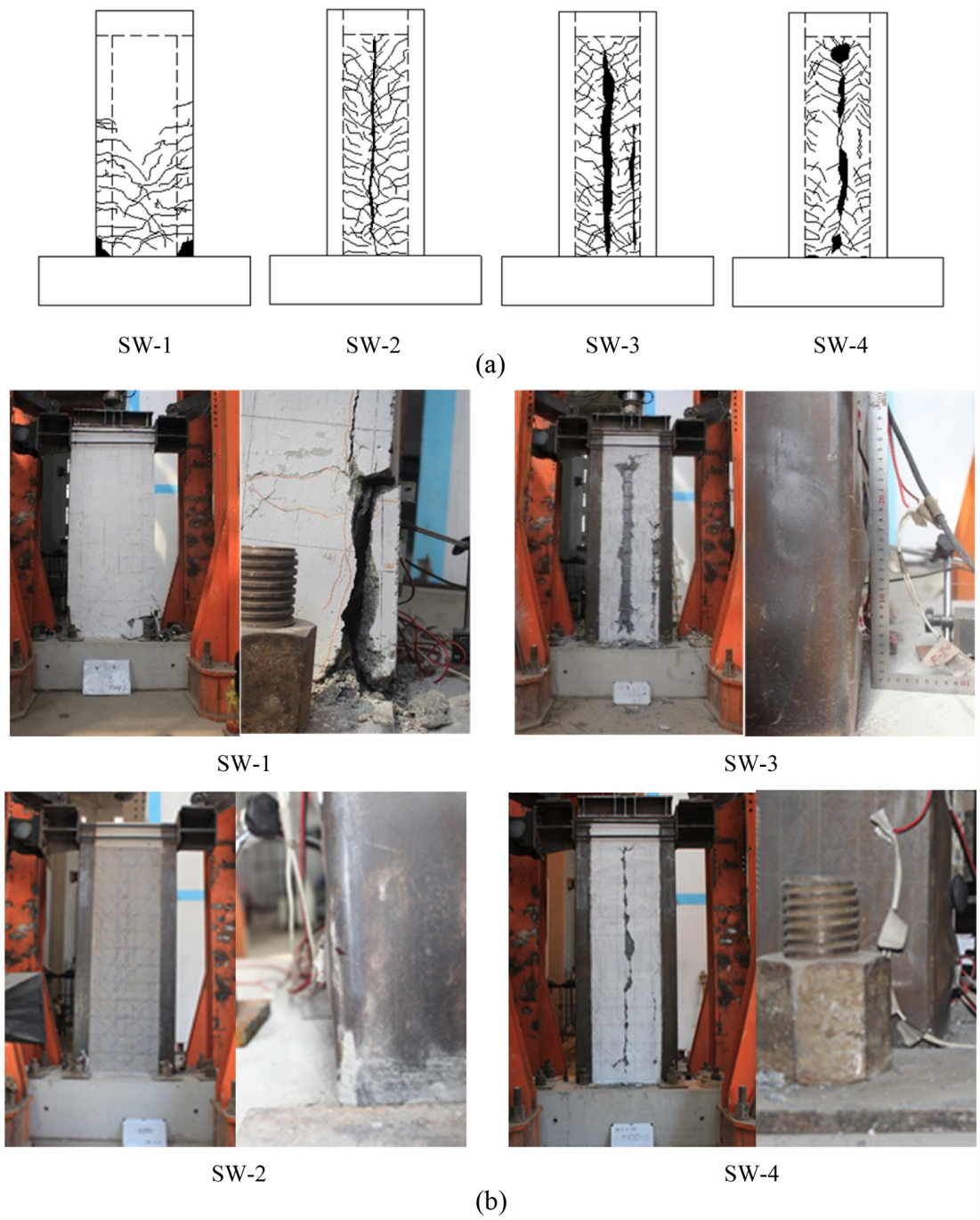

Figure 6. Experimental phenomenon of testing specimens (drift ratio: 1/50): (a) crack patterns of specimen and (b) failure modes.

axial compression ratio in this test is large enough to represent the values in practical cases.

Testing results

Failure modes

This part describes the experimental phenomenon of all testing specimens, with a particular attention paid on the failure mode.

Figure 6(a) plots the crack patterns, and Figure 6(b) shows the failure modes of SW specimens .SW-1 is the conventional SW, which shows concentrated cracks at the lower part of the specimen. The first horizontal crack had a width of 0.03 mm, occurred in the boundary columns 300 mm above the baseline, when the roof drift was up to 4.65 mm corresponding to 1/613. As the drift loading increased, the horizontal cracks propagated from the boundary columns to the wall.

Table 3. Comparisons of characteristic points and ductility.

Specimen no.	F_c/kN	Δ_c/mm	F_y/kN	Δ_y/mm	F_u/kN	Δ_u/mm	F_p/kN	Δ_p/mm	θ	μ
SW-1	245.75	4.65	36.58	14.09	357.17	41.43	418.86	23.53	1/69	2.94
SW-2	259.48	6.00	322.73	9.28	459.06	65.34	543.51	35.18	1/43	7.04
SW-3	293.76	7.10	515.73	14.95	537.90	57.23	632.33	23.53	1/50	3.83
SW-4	500.97	7.80	605.50	13.95	546.98	51.40	643.50	14.20	1/55	3.68

SW: shear wall.

When the drift reached to 14 mm corresponding to 1/200, the vertical steel rebars in the tensile zone yielded, leading to cross inclined cracks in the middle of the wall, with a maximum width up to 0.3 mm. At the end of the test, the maximum width of cracks near to the bottom of wall was as large as 10 mm; significant concrete crushing was observed at 400 mm from the edges of the wall base; steel rebars also buckled. When the further drift was increased to 67.05 mm corresponding to 1/43, the strength capacity which represents the lateral force decreased to 85% of the peak value, the testing was terminated. This specimen was able to sustain several loading cycles after the vertical steel rebars in the boundary columns buckled, and it finally failed due to the progressive loss of shear strength capacity, indicating the failure mode is the flexural-shear type.

Regarding with CFST-CSW specimens, they displayed similar crack propagation and failure mode. The description of the testing results of CFST-CSWs takes SW-3 as an example. Compared with conventional SW (i.e. SW-1), SW-3 produced uniformly distributed crack pattern, as shown in Figure 6(a). The first crack occurred at the connection zone between the studs and RC wall, which was about 300–700 mm away from the edge of the wall base, when the top displacement reached 7.1 mm corresponding to a drift ratio of 1/400. The delayed crack implied a higher global strength capacity of SW-3 than SW-1. It is noted the middle part of the RC wall cracked when the top displacement reached 7.1 mm because the concrete cover of steel plate connector is only 20 mm. Such a thin concrete cover lead to early crushing and spalling, which can be avoided by increasing the concrete cover thickness. As the displacement was up to 14.95 mm corresponding to a drift ratio of 1/190, the steel tube in the compressive zone yielded, the crack widened, and the cross inclined cracks formed. In the further loading cycle to 24 mm corresponding to a drift ratio of 1/120, the steel tube in the compressive zone buckled 70 mm away from the edge of the wall base. Concrete spalling was found in the middle of the RC wall. At the end of the loading, the top displacement reached 57.23 mm corresponding to a drift ratio of 1/50, the steel tube buckled again, significant concrete spalling was noticed in the middle of the RC wall. The loading was terminated upon the strength capacity was lower than 85% of the peak value. During the entire loading history, the slip between SW and steel tube was smaller than 2 mm, indicating a good composite behavior. It is worth noting that the steel plate connector prevented long inclined cracks to cross the whole wall, while producing many minor cracks. The effect of changing the axial compression ratio is investigated. The drift ratio corresponding to the first crack of SW-2, SW-3, and SW-4 is 1/77, 1/400, 1/590, respectively. Thus, a high axial compression ratio leads to early occurrence of the first crack.

Strength capacity and ductility

Table 3 shows the measured crack loads F_c, yield loads F_y, peak loads F_p, and ultimate loads F_u of the specimens. The F_c is defined as the load corresponding to the occurrence of the first crack. The yielding behavior is usually caused by the yielding of steel rebars or tubes, and the associated yielding strength is denoted as F_y. F_p refers to the peak strength capacity in the loading history. F_u equals to 85% of the F_p. With the characteristic points of strength defined, the associated displacement can be readily extracted from the loading curve. $\theta = \Delta_u/H$ and $\mu = \Delta_u/\Delta_y$ are the ultimate drift ratio and ductility, respectively, where H is measured from the loading point to the wall base, $H = 2850$ mm.

According to Table 3, several trends are observed: (1) upon the identical axial compression ratio, CFST-CSW displays higher crack, yield, and peak strength capacity than conventional SW by 20.00%, 40.91%, and 50.96%, respectively. In addition, CFST-CSW shows larger ultimate deformation capability and ductility than conventional SW by 34% and 30%, respectively. Thus, CFST-CSW has better strength capacity and ductility than conventional SW. (2) When the axial compression ratio increases from 0 to 0.15, the crack, yield, and peak strength capacity of CFST-CSW increase by 13.21%, 59.94%, and 16.39%, respectively, and the increments become 70.54%, 17.48%, and 1.77% when the axial compression ratio increases from 0.15 to 0.28. It indicates that the increase of the axial compression ratio could improve the strength capacity

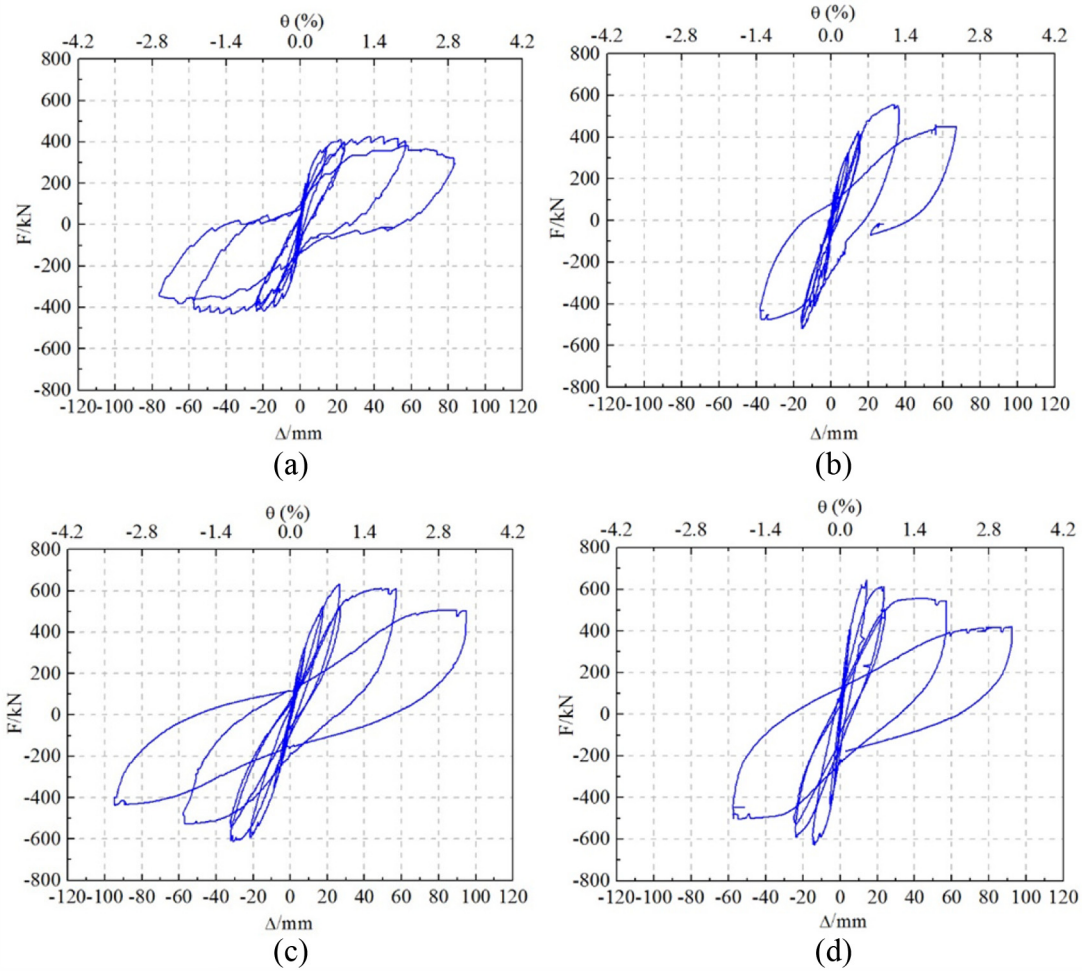

Figure 7. Hysteretic curves of specimens: (a) SW-1, (b) SW-2, (c) SW-3, and (d) SW-4.

of CFST-CSW but this influence is relatively small when it comes to high axial compression ratio. It is worth noting that the influence of axial compression ratio for crack strength capacity is always remarkable. (3) As the axial compression ratio increases, SW-3 and SW-4 show smaller ultimate deformation capability than SW-2 by 12.42% and 21.33%, respectively, while the ductility decreases by 45.60% and 47.73% than SW-2. It indicates that the ductility capacity of CFST-CSW will decease with the increase of the axial compression ratio. (4) SW-4 shows 25.17% larger ductility and 24.06% larger ultimate deformation capability than SW-1, this comparison further indicates that the CFST-CSW has a better seismic capacity than conventional SW, even if the former was subjected to a larger axial compression ratio.

Hysteresis and skeleton curves

Figure 7 presents the hysteresis curves of all specimens. It is seen that the specimens show linear elastic behavior in the initial loading history, and then they generate noticeable plastic behavior with energy dissipated. With the applied load further increased, stiffness and strength degradation is observed. The difference between conventional SW and CFST-CSW can be observed by comparing SW-1 and SW-3, which were under identical axial compression ratio. It is clear that SW-3 shows wider hysteresis and milder pinching behavior, indicating better seismic capacity. The accumulated dissipated energy of SW-3 is 72034 kN mm, which is higher than that of SW-1 by 41.04%. The effect of axial compression ratio is also assessed by comparing SW-3 with SW-4. The hysteresis shape and enclosed area are slightly affected by increasing axial compression ratio, while strength degradation is deteriorated. The accumulated dissipated energy of SW-3 and SW-4 are 72034 and 77402 kN mm, respectively, which are similar with each other, and it can be attributed to that the influence of axial compression ratio for the strength capacity and ductility of CFST-CSW is relatively small when it comes to high axial

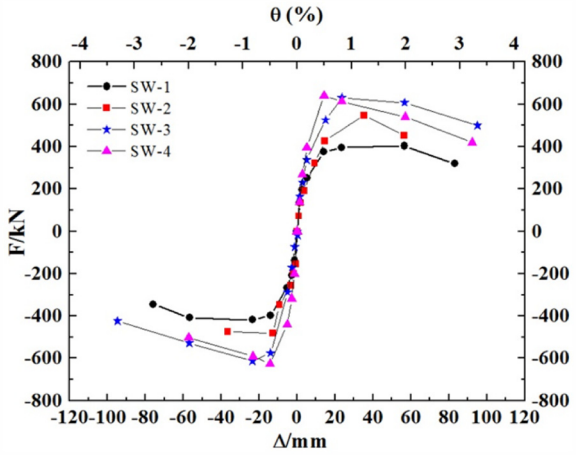

Figure 8. Skeleton curves of SW-1/2/3/4.

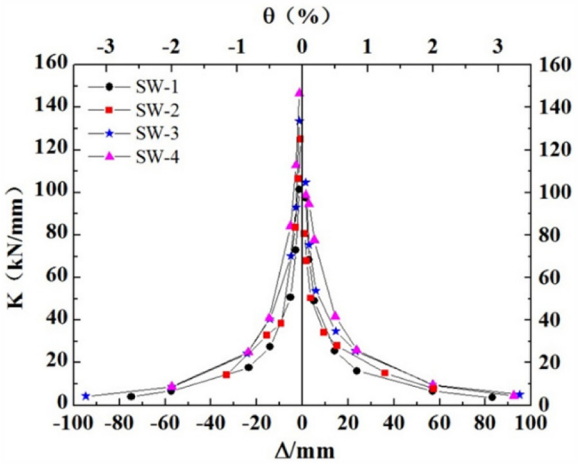

Figure 9. Stiffness degradation of specimens.

compression ratio. Parenthetically, the loading scheme on SW-2 was misconducted. Thus, a direct comparison between SW-2 with the other specimens is not made.

Figure 8 assembles the skeleton curves, which are essentially the envelop curves of hysteresis curves. It is clear that the specimens display close linear elastic behavior initially. With the loading increased, the specimens cracked, leading to a noticeable yielding plateau and stiffness degradation. However, it is seen that the post-yielding stiffness and strength of CFST-CSW are noticeably higher than that of conventional SW. The significant strength deterioration after peak capacity of SW-4 is due to the high axial compression ratio.

Stiffness degradation

To investigate the stiffness degradation of the specimens, Figure 9 plots the secant stiffness as a function of the displacement. The secant stiffness is defined as the ratio of the peak strength in each loading cycle to the corresponding displacement. It is seen the stiffness is symmetrical in positive and negative directions during the entire loading history, irrespective of the SW types. In the initial loading stage, SW-4 shows higher stiffness, indicating that the axial compression ratio contributes to the increase of stiffness. CFST-CSW displays higher stiffness than conventional SW from the elastic state to significant plastic state. Table 4 lists the stiffness corresponding to elastic, crack, yield, peak, and ultimate loads, denoted as K_o, K_c, K_y, K_p, and K_u, respectively. It is seen that the stiffness of CFST-CSW degrades at a lower rate than that of conventional CSW. The axial compression ratio also affects this parameter by increasing initial stiffness while deteriorating stiffness when the specimen was significantly damaged.

Table 4. Stiffness degradation coefficient of specimens.

Specimen no.	K_y/K_0	K_p/K_0	K_u/K_0
SW-1	0.36	0.24	0.12
SW-2	0.47	0.21	0.09
SW-3	0.41	0.32	0.11
SW-4	0.42	0.44	0.10

SW: shear wall.

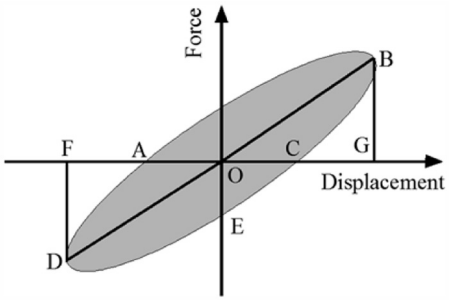

Figure 10. Determination of equivalent damping ratio.

Energy dissipation capacity

The energy dissipation capacity of specimens is quantified by the equivalent damping ratio

$$\varsigma_e = \frac{1}{2\pi}\frac{S_{(ABC+CDA)}}{S_{(OBG+OFD)}} \quad (2)$$

where the parameters are shown in Figure 10. $S_{(ABC+CDA)}$ refers to the area bounded by hysteretic loop of each cycle, representing the dissipated energy

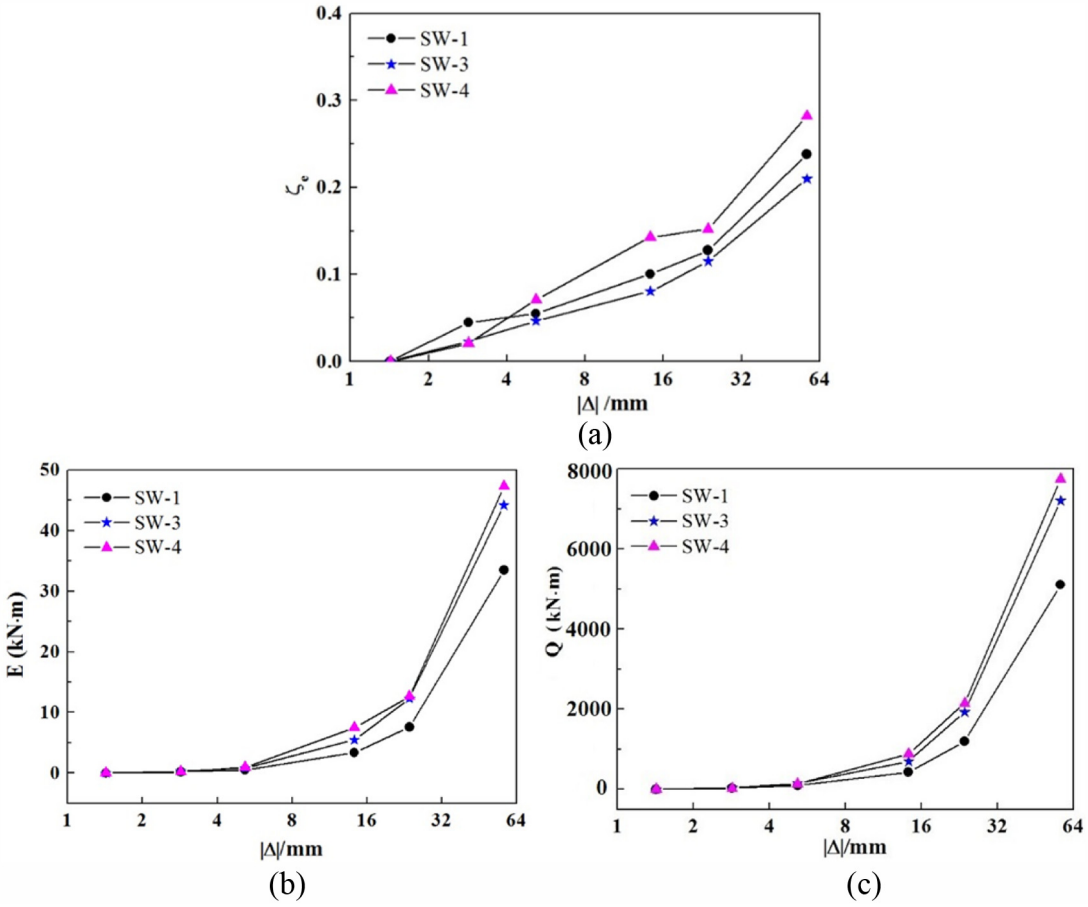

Figure 11. Energy dissipation capacity: (a) equivalent damping ratio, (b) dissipated energy of each cycle, and (c) accumulated dissipated energy.

in each loading cycle. $S_{(OBG + OFD)}$ is the strain energy, which is calculated from the secant stiffness determined by experiment. SW-2 is not included in this analysis, due to the different loading history. As shown in Figure 11(a), ζ_e increases rapidly with the accumulation of plastic deformation in the specimens. SW-4 shows the highest damping behavior among the considered specimens, and its ζ_e is up to approximate 0.3 in the final loading cycle which indicates a high energy dissipation capacity. SW-1 and SW-3 display comparable damping behavior. SW-3 shows a slight lower ζ_e than SW-1 because of its higher strength capacity.

Figure 11(b) presents the dissipated energy for each specimen. The dissipated energy (E) in each cycle was evaluated from the horizontal load versus horizontal total drift hysteretic curves, as the area bounded by hysteretic loop of each cycle. The dissipated energy is negligible before the SW cracks since the specimens are mainly in elastic stage. After the SW cracks, the dissipated energy increases rapidly with the accumulation of plastic deformation in the specimens. CFST-CSWs always dissipate more energy than the conventional SW throughout the testing program. For example, at the final cycle, the dissipated energy of SW-3 and SW-4 is 31.94% and 41.22% higher than that of SW-1, respectively. This can be attributed to the higher strength capacity, the better ductility, and more uniform crack pattern of the CFST-CSW specimens. Similar observations can be made by plotting the accumulated dissipated energy, as shown in Figure 11(c).

Lateral loading capacity

Formulation for strength capacity

Flexural failure occurred for all the specimens, so the lateral loading capacity could be calculated from the flexure strength at the wall base section. Several hypotheses are introduced. (1) Plane section is assumed to remain plane after deformation. (2) The tensile behavior of concrete and the compressive behavior of steel are not considered. (3) The stress of concrete in the compression zone was calculated by using the

Table 5. Comparison of experimental and calculated results of ultimate capacity.

Specimen no.	F_m	F_c	$(F_m - F_c)/F_m$	F_s	$(F_m - F_s)/F_m$
SW-2	543.51	489.56	9.93%	475.79	12.46%
SW-3	632.33	628.77	0.56%	623.86	1.34%
SW-4	643.50	701.20	−8.97%	659.65	−2.51%

SW: shear wall.

equivalent rectangular stress block of average stress αf_c and the extent of βx, where α and β are two parameters of the equivalent rectangular stress block, x is the depth of concrete in the compression zone, and f_c is 0.76 f_{cu}, where f_{cu} is the measured cubic compressive strength of concrete. When it comes to C30 concrete, α is 1.0 and β is 0.8. (4) The steel tubes in compression and tensile zone and the steel rebars in tensile zone all reach yield strength. Only the steel rebars which are h_w-1.5 x distant from the tensile side are considered.

The cross-sections of the specimens are subdivided into several fibers including concrete fibers, steel fibers, and reinforcement fibers. The calculation model is shown in Figure 12.

According to the force equilibrium and moment equilibrium with respect to the wall's centroid, the following equations were established

$$N_{sw} = f_{yw} b_w \rho_w (h_w - 1.5x - h_f) \tag{3}$$

$$N_{c2} = f_{c2} A_c \tag{4}$$

$$N_{c1} = f_{c1} b_w (0.8x - h_f) \tag{5}$$

$$N + f_a A_a = N_{c1} + N_{c2} + f_a A_a - N_{sw} \tag{6}$$

$$M = f_a A_a (h_w - h_f) + 0.5 N_{c1} (h_w - 0.8x - h_f) + 0.5 N_{c2} (h_w - h_f) + 0.5 N_{sw} (1.5x - h_f) \tag{7}$$

where N and M are the axial force and bending moment, respectively; N_{c1} and N_{c2} are compression of internal and external concrete of steel tube; N_{sw} is the tensile force of steel rebars in the tension zone; x is the height of the compressive concrete; f_{yw} and ρ_w are the yield strength and reinforcement ratio of the vertical steel rebars. f_a, A_a, f_c, and A_c are the same as to the definition in equation (1).

With equations (3) to (6), x is obtained. Substituting x into equation (7), the bending moment M is calculated. The horizontal loading capacity F_j is calculated as below

$$F_c = \frac{M - N\Delta_p}{H} \tag{8}$$

where H is measured from the loading point to the wall base, H = 2850 mm; Δ_p is the lateral displacement corresponding to the peak strength capacity. The

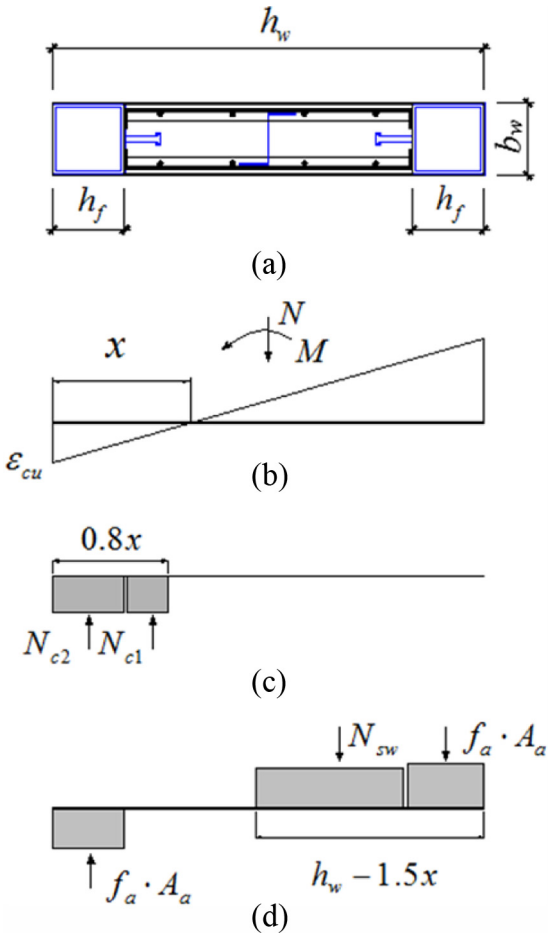

Figure 12. Mechanism of the flexural behavior of CFST-CSW: (a) cross-section, (b) strain, (c) concrete part, and (d) steel part.

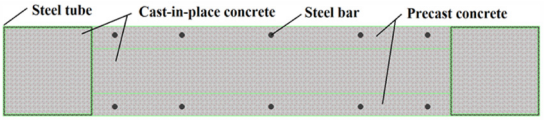

Figure 13. The cross-section model of CFST-CSW.

calculated maximum strengths F_c and measured maximum strengths F_m are compared in Table 5. The calculated results correlate well with the test results for most of the specimens with an error within 10%, and

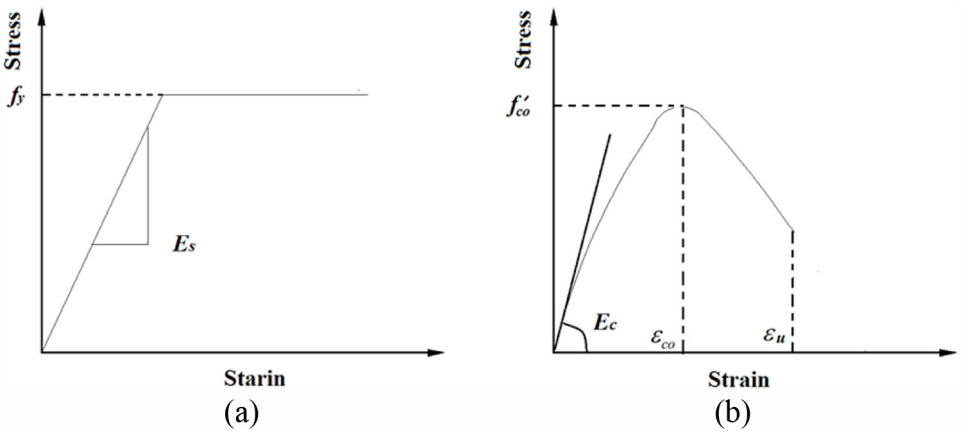

Figure 14. The constitutive relation of the material: (a) steel and (b) concrete.

the strengths tend to be overestimated by the proposed analytical model when the axial compression ratio is high.

Simulation analysis for strength capacity

Simulation analyses are added using the analysis software XTRACT, which is always used to assess the moment capacity of a cross-section (Chadwell and Imbsen, 2004). The simulation model of the wall base section is shown in Figure 13. The constitutive relation of steel is bilinear steel model without strain hardening as shown in Figure 14(a). The yield strength and elastic modulus of the steel are the measured values. The constitutive relation of concrete is unconfined concrete model (Mander et al., 1988) as shown in Figure 14(b). The $f_c{}'_o$ is the cylinder compressive strength of the concrete, ε_{co} is the strain, E_c is the elastic modulus of concrete, and ε_u is the crushing strain.

The ultimate lateral loading capacity calculated by the simulation analysis is listed in Table 5. The simulation results correlate well with the test results for most of the specimens with an error less than 13%, which indicates that the simulation technique is reasonably accurate.

Conclusion

This study proposed a new type of precast SW, that is, CFST-CSW. To investigate the seismic capacity of this new SW, cyclic loading tests were conducted on three full-scale specimens, a conventional SW was also tested for comparison purpose. Several conclusions are made as follows:

1. Current CFST-CSW and conventional SW displayed shear-flexural failure mode, whereas CFST-CSW generated a more favorable crack pattern which distributed over the entire wall.
2. Upon a same axial compression ratio, CFST-CSW is superior to conventional SW in both strength capacity and ductility. In particular, when the axial compression ratio is 0.15, CFST-CSW shows a higher crack, yield, and peak strength capacity than conventional SW by 20.0%, 41.0%, and 51.0%, respectively; the ultimate deformation and ductility are larger by 34.6% and 30.0%.
3. As the axial compression ratio increased, the strength capacity and initial stiffness of CFST-CSW increased to a certain degree, whereas the ultimate deformation and ductility decreased slightly, and the dissipated energy was nearly unaffected.
4. Even if the CFST-CSW was subjected to a larger axial compression ratio than conventional SW, the former still showed a larger ultimate deformation capacity, ductility and energy dissipation capacity, indicating a better seismic capacity.
5. Both the empirical prediction model and simulation analysis model predict the ultimate lateral loading capacity of CFST-CSW very well, with an error less than 13%.

Acknowledgement

However, any opinions, findings, conclusions, and recommendations presented in this paper are those of the authors and do not necessarily reflect the views of the sponsors.

Declaration of Conflicting Interests

The author(s) declared no potential conflicts of interest with respect to the research, authorship, and/or publication of this article.

Funding

The author(s) disclosed receipt of the following financial support for the research, authorship, and/or publication of this article: This research was supported by the General Program of National Natural Science Foundation of China under award no. 51578324, the Fundamental Research Funds of Shandong University (grant no.: 31410076614125), and the National "Twelfth Five-Year" Plan for Science & Technology Support of China (grant no.: 2015BAL03B01).

References

ACI 318-14 (2014) *Building Code Requirements for Structural Concrete and Commentary*. Farmington Hills, MI: American Concrete Institute.

Cao WL, Xue SD and Zhang JW (2003) Seismic performance of RC shear walls with concealed bracing. *Advances in Structural Engineering* 6(1): 1–13.

Cao WL, Zhang JW, Xue SD, et al. (2006) Seismic performance of RC coupled short-pier shear walls with concealed bracing. *Advances in Structural Engineering* 9(4): 577–589.

Chadwell CB and Imbsen RA (2004) XTRACT: a tool for axial force–ultimate curvature interactions. Available at: https://ascelibrary.org/doi/pdf/10.1061/40700(2004)178

Chen ZH, Jiang YT, Zhang XM, et al. (2016) Parametric analysis and calculation method for bending and shear capacities of innovative composite shear walls. *Advances in Structural Engineering* 20: 1046–1058.

Clough RW, Malhas F and Oliva MG (1989) Seismic behavior of large panel precast concrete walls: analysis and experiment. *PCI Journal* 34(5): 42–66.

Eom TS, Park HG, Lee CH, et al. (2009) Behavior of double skin composite wall subjected to in-plane cyclic loading. *Journal of Structural Engineering* 135(10): 1239–1249.

GB50011-2010 (2010) *Code for Seismic Design of Buildings* (National Standard of People's Republic of China). Beijing, China: China Architecture & Building Press (in Chinese).

Hossain KMA and Wright HD (2004) Experimental and theoretical behaviour of composite walling under in-plane shear. *Journal of Constructional Steel Research* 60(1): 59–83.

Hu HS, Nie JG, Fan JS, et al. (2016) Seismic behavior of CFST-enhanced steel plate-reinforced concrete shear walls. *Journal of Constructional Steel Research* 119: 176–189.

Japan Building Standards Law (2002) Law No.85, 2002.7.12 (in Japanese).

Liao FY, Han LH and Tao Z (2009) Seismic behaviour of circular CFST columns and RC shear wall mixed structures: experiments. *Journal of Constructional Steel Research* 65(8–9): 1582–1596.

Liao FY, Han LH and Tao Z (2012) Performance of reinforced concrete shear walls with steel reinforced concrete boundary columns. *Engineering Structures* 44: 186–209.

Looi DTW, Su RKL, Cheng B, et al. (2017) Effects of axial load on seismic performance of reinforced concrete walls with short shear span. *Engineering Structures* 151: 312–326.

Luo Y, Guo X, Li J, et al. (2015) Experimental research on seismic behaviour of the concrete-filled double-steel-plate composite wall. *Advances in Structural Engineering* 18(11): 1845–1858.

Mander JB, Priestley MJN and Park R (1988) Theoretical stress-strain model for confined concrete. *Journal of Structural Engineering* 114(8): 1804–1826.

Polat G (2008) Factors affecting the use of precast concrete systems in the United States. *Journal of Construction Engineering and Management* 134(3): 169–178.

Priestley MJN and Tao JR (1993) Seismic response of precast prestressed concrete frames with partially debonded tendons. *PCI Journal* 38(1): 58–69.

Wang D and Lv XL (2010) Progress of study on seismic perform of precast concrete shear wall systems. *Structure Engineers* 26(6): 128–134 (in Chinese).

Xiao QD and Guo ZX (2014) Quasi-static test for double-wall precast concrete short-leg shear walls. *Journal of Harbin Institute of Technology* 46(12): 84–88 (in Chinese).

Zhang HM, Lu XL, Duan YF, et al. (2014) Experimental study on failure mechanism of RC walls with different boundary elements under vertical and lateral loads. *Advances in Structural Engineering* 17(3): 361–380.

Zhang Y and Wang Z (2000) Seismic behavior of reinforced concrete shear walls subjected to high axial loading. *ACI Structural Journal* 97(5): 739–750.